

Combined Estimation of Ionospheric Effects in SAR Images exploiting Faraday Rotation and Autofocus

Valeria Gracheva, *Member, IEEE*, Jun Su Kim, Pau Prats-Iraola, *Senior Member, IEEE*, Rolf Scheiber, and Marc Rodriguez-Cassola

Abstract—At lower frequencies, synthetic aperture radar (SAR) images can be significantly affected by ionospheric scintillations. This letter proposes an approach to estimate ionospheric artifacts in single SAR images by combining Faraday rotation estimates and autofocus methods by using a Wiener filter. This novel approach achieves a superior performance when compared to using these techniques independently. This improvement is demonstrated by injecting randomly simulated ionospheric phase screens into simulated point targets and airborne data adjusted to the parameters of the Biomass system.

Index Terms—Ionospheric scintillations, SAR, Faraday rotation, autofocus.

I. INTRODUCTION

The ionosphere, which is defined as the ionized part of the Earth's upper atmosphere, impacts synthetic aperture radar (SAR) images, especially at lower frequencies (P band, L band). The main ionospheric effects on SAR are geolocation errors (both in the range and azimuth dimensions), range and azimuth defocusing, as well as the distortion of the scattering matrix of the targets due to the so-called Faraday rotation (FR) effect [1]. The turbulent part of the ionosphere, the so-called ionospheric scintillations, occurs mainly in low and high latitude regions [2] and it corrupts the azimuth impulse response functions [3]. It has been previously proposed to use autofocus to estimate the azimuth defocusing due to ionospheric scintillations [4] and to exploit the phenomenon of Faraday rotation (FR) to estimate them in high-latitude regions [5]. This paper focuses on combining both techniques, autofocus and FR, to improve the estimation of ionospheric scintillations.

ESA's Earth Explorer 7 Biomass mission is a clear candidate for the usage of the proposed approach, which will be the first spaceborne SAR mission operating at P band. The ground processor of the Biomass mission will include an ionospheric mitigation step for single-look complex SAR images, where the ionosphere is estimated from the FR and also autofocus will be optionally performed [6]. Both estimation techniques are therefore already available and the effort to combine them should be marginal.

In [7] the split-spectrum method, which uses two range subband interferograms, and the estimation of mutual azimuth shifts between two images due to the ionosphere are combined to achieve an improved estimation of the ionospheric effects from InSAR images. In this contribution we suggest a combination approach which is similar to the one proposed in [7], but developed for different methods and single-look complex SAR images instead of for interferometric pairs.

This paper is organized as follows: Section II describes the FR, autofocus and combined estimation approaches. To evaluate and compare these methods, power law ionospheric phase screens are simulated and injected into data in Section III. Section III-A presents the rationale to simulate the ionospheric phase screens. In Section III-B point targets with Biomass system parameters are simulated to examine the performance of the investigated methods. To evaluate the three techniques on distributed targets and rate them in a more realistic environment, real airborne data acquired at P band by DLR's F-SAR sensor are adjusted to Biomass system parameters in Section III-C. Section IV concludes this paper.

II. IONOSPHERIC PHASE SCREEN ESTIMATION METHODS

A. FR Estimation Approach

The polarization of non-circularly polarized radio waves is changed when traversing the ionosphere, an effect known as FR. In this paper the Bickel and Bates estimator [8] is used to estimate ionospheric scintillations from FR. Following the work in [5], the variance of a single-look estimate is

$$\sigma_F^2 = \frac{C^2}{16} \left(\pi^{2/3} - \pi \sin^{-1}(\rho) + (\sin^{-1}(\rho))^2 - \frac{Li_2(\rho^2)}{2} \right), \quad (1)$$

where $\rho = \frac{SNR}{1+SNR}$, with SNR being the signal-to-noise ratio and $Li_2(\cdot)$ is the Euler dilogarithm. $C = \frac{4\pi m_e f}{e \vec{B} \cdot \hat{k}}$ is the proportionality factor between the ionospheric phase screen and the FR angle. Here e and m_e are the charge and mass of an electron, \hat{k} is the unit wave propagation vector, \vec{B} is the geomagnetic field and f is the carrier frequency.

Under the assumption of the thin ionospheric layer model [9], FR can be exploited to estimate the ionospheric phase screen as

$$\hat{\varphi}_F = \mathbf{H}_G(\varphi + \mathbf{n}_F), \quad (2)$$

with φ being the true phase screen and $\mathbf{n}_F \sim \mathcal{N}(0, \sigma_F^2)$ is noise due to the FR estimation uncertainty. \mathbf{H}_G represents the 2D convolution matrix of a rotated Gaussian filter, which is applied to denoise the estimation. A rotation of the filter, which is computed based on the orientation angle of the magnetic field plane and the acquisition geometry, is in general recommended in order to better filter the scintillations [5]. $\hat{\varphi}_F$, φ and \mathbf{n}_F are vectors with dimensions $N_r N_{x_i} \times 1$, where N_r is the number of slant range samples and N_{x_i} the number of azimuth samples at the ionospheric height. \mathbf{H}_G has the dimensions $N_r N_{x_i} \times N_r N_{x_i}$.

B. Autofocus Estimation Approach

Autofocus measures the error in the Doppler rate, here caused by ionospheric scintillations, which is proportional to the second derivative of the ionospheric phase screen. In this paper map-drift autofocus is used [10], which is a commonly used autofocused method since it does not rely on the presence of point-like scatterers in the observed scene, i.e., it relies on the image contrast. The map-drift autofocus is based on the estimation of the mutual shift between two azimuth sub-looks of a SAR image. If no phase errors are present, the two sub-look images will be perfectly aligned. However, in the presence of a more-than-linear order phase error within the synthetic aperture, an azimuth shift will arise between the sub-look images, which can be measured, e.g., using image cross-correlation techniques.

The relationship between the estimated Doppler rate error $\Delta\hat{\mathbf{k}}$ and the true phase screen φ can be described as

$$\Delta\hat{\mathbf{k}} = \mathbf{H}_A \varphi + \mathbf{n}_A, \quad (3)$$

where $\mathbf{n}_A \sim \mathcal{N}(0, \sigma_A^2)$ denotes noise due to the autofocus estimation uncertainty. The noise variance σ_A^2 can be estimated from the variance of $\Delta\hat{\mathbf{k}}$ within a small window (e.g., 3×3 samples) by assuming that the Doppler rate error is not changing significantly within this window. $\Delta\hat{\mathbf{k}}$ and \mathbf{n}_A have the dimensions $N_r N_{x_g} \times 1$, where N_{x_g} is the number of azimuth samples on ground. \mathbf{H}_A is a convolution matrix of the autofocus filter, which for the map-drift autofocus is a convolution between the second derivative filter and a lowpass filter, where the latter represents the averaging effect within the length of the synthetic aperture at ionospheric height. \mathbf{H}_A has the dimensions $N_r N_{x_g} \times N_r N_{x_i}$. To estimate the phase screen from autofocus, an inverse filter matrix has to be applied to the Doppler rate error vector

$$\hat{\varphi}_A = \mathbf{H}_{invA} \Delta\hat{\mathbf{k}}. \quad (4)$$

This inverse filter matrix can be derived by finding the minimum variance between the true and estimated phase screen, which leads to the Wiener filter

$$\mathbf{H}_{invA} = (\mathbf{H}_A \mathbf{C}_{\varphi\varphi} \mathbf{H}_A^T + \sigma_A^2 \mathbf{I}_{N_r N_{x_g}})^{-1} \mathbf{H}_A \mathbf{C}_{\varphi\varphi}. \quad (5)$$

Here $\mathbf{I}_{N_r N_{x_g}}$ is the identity matrix with dimensions $N_r N_{x_g} \times N_r N_{x_g}$ and $\mathbf{C}_{\varphi\varphi} = E\{\varphi\varphi^T\}$ is the matrix form of the ionospheric phase screen autocorrelation function with the dimensions $N_r N_{x_i} \times N_r N_{x_i}$. In practice the ionospheric phase screen autocorrelation function is not known and needs to be estimated from the data or a model of the autocorrelation function has to be assumed and the unknown parameters have to be retrieved. In this paper a power law spectrum is assumed, leading to an autocorrelation function as described in Section III-A. To estimate the unknown parameters of this function, the autocorrelation of the FR estimation and the autocorrelation of the Gaussian filter are used. Note that the performance of the autofocus estimation approach and the combined estimation

approach, which will be described in the next subsection, relies on the correct retrieval of the ionospheric phase screen autocorrelation function.

C. Combined Estimation Approach

For the combined estimation method, the ionospheric phase screen is estimated from

$$\hat{\varphi}_C = \mathbf{H}_{invC} \begin{pmatrix} \hat{\varphi}_F \\ \Delta\hat{\mathbf{k}} \end{pmatrix}, \quad (6)$$

where the inverse filter matrix \mathbf{H}_{invC} is specified in equation (7). It was derived by using the same approach as for the autofocus estimation technique in Section II-B. The dimensions of \mathbf{H}_{invC} are $N_r N_{x_i} \times N_r(N_{x_i} + N_{x_g})$.

III. SIMULATION RESULTS

A. Ionospheric Phase Screen Simulation

A common method to generate ionospheric phase screens is by filtering zero-mean Gaussian random fields with a given power law spectral density function [3], [11], [12]. The according autocorrelation function is equal to [13]

$$R_{\varphi\varphi}(\Delta r, \Delta x_i) = G \frac{r_e^2 \lambda_r^2}{\cos \beta} C_k L \left(\frac{2\pi}{1000} \right)^{2\nu+1} \left| \frac{y(\Delta r, \Delta x_i)}{4k_0} \right|^{\nu-1/2} \frac{K_{\nu-1/2}(k_0 y(\Delta r, \Delta x_i))}{\Gamma(\nu+1/2)}. \quad (8)$$

Here Δr is the slant range shift, Δx_i the azimuth shift at ionospheric height, G is a geometric enhancement factor, r_e the classical electron radius, β the ray nadir angle at an ionospheric piercing point, $C_k L$ the vertically integrated turbulence strength at 1-km scale and ν is the spectral index parameter. The distance function $y(\Delta r, \Delta x_i)$, which is derived in [13], depends on the anisotropy elongation factors a , b and the orientation angle of the magnetic field plane. The gamma function is denoted by $\Gamma(\cdot)$, $K_\nu(\cdot)$ is the modified Bessel function and $k_0 = \frac{2\pi}{l_0}$, where l_0 is the outer scale size, which is typically around 10 km [9].

The parameters of $R_{\varphi\varphi}(\Delta r, \Delta x_i)$ used in this paper are summarized in Table I. The selected spectral index parameter is the one that has been selected as reference value for the Biomass mission and the sampling corresponds to that of single-look Biomass products. The chosen anisotropy elongation factors were reported in [14] to occur during night for high latitude areas. The orientation of the magnetic field plane was calculated for the latitude 70 N and longitude 84 E with the Biomass geometry. A realistic integrated strength of turbulences ($C_k L$) for high latitudes and strong ionospheric scintillations is used [17]. It is assumed that the ionospheric phase screen is originated from a single layer at a height of about 350 km altitude [8].

$$\mathbf{H}_{invC} = \begin{pmatrix} \mathbf{H}_G (\mathbf{C}_{\varphi\varphi} + \sigma_F^2 \mathbf{I}_{N_r N_{x_i}}) \mathbf{H}_G^T & \mathbf{H}_A \mathbf{C}_{\varphi\varphi} \mathbf{H}_G^T \\ \mathbf{H}_G \mathbf{C}_{\varphi\varphi} \mathbf{H}_A^T & \mathbf{H}_A \mathbf{C}_{\varphi\varphi} \mathbf{H}_A^T + \sigma_A^2 \mathbf{I}_{N_r N_{x_g}} \end{pmatrix}^{-1} \begin{pmatrix} \mathbf{H}_G \mathbf{C}_{\varphi\varphi} \\ \mathbf{H}_A \mathbf{C}_{\varphi\varphi} \end{pmatrix}. \quad (7)$$

TABLE I
PARAMETERS FOR IONOSPHERIC PHASE SCREEN SIMULATION

Integrated strength of turbulence	$10^{32.00}$
Spectral index parameter	1.325
Outer scale size	10 km
Anisotropy elongation factors (a, b)	8, 4
Orientation of magnetic field plane	26.42°
Ionospheric phase screen altitude	350 km
Slant range sampling	19.81 m
Azimuth sampling	4.24 m

B. Simulation Results based on Point Targets

To test the different approaches and evaluate the impact of ionospheric scintillations on point targets, a scene with 2400 point targets was simulated, where the parameters and the orbit of the simulation were chosen to match the Biomass mission. The carrier frequency of the Biomass mission is at 435 MHz, the range and azimuth bandwidths are 6 MHz and 850 Hz respectively, a center slant range of 760.88 km is assumed and the satellite altitude is at 675.80 km. Here a signal-to-noise ratio (SNR) of 18 dB was used. A total of 100 ionospheric phase screens were generated randomly, as outlined in Section III-A, and injected into the simulated data at ionospheric height, as described in [5]. For each phase screen generation, the autofocus approach was applied by refocussing the data back to ground height and estimating the Doppler rate error of each point target with map-drift autofocus. From the Doppler rate error the phase screen of each generation was estimated by using (4).

The FR estimation approach was tested by adding random noise with variance calculated by equation (1) to the same 100 phase screens and then filtering the result with a rotated Gaussian filter, as described by equation (2), and downsampling to match the sampling rate of the autofocus estimation. The estimated Doppler rate error and the estimated phase screen with the FR approach of each phase screen generation are then used to perform the combined estimation approach by applying (6).

The results of this evaluation are summarized in Tables II and III. In Table II the mean and standard deviation of variances between estimated phase screens ($\hat{\varphi}$) for each approach and the true phase screens of the 100 runs are displayed. Table II shows that the lowest variance can be achieved with the combined estimation method.

One phase screen estimation example is displayed in Figure 1. Figure 1 (a) shows the simulated phase screen and Figures (b)-(d) display the estimated phase screens with the three different methods. Figure 1 (d) clearly shows that the combined estimation approach provides the best result by benefiting from the FR and autofocus method.

In Table III the impact of the ionospheric scintillations on the azimuth impulse response function and their improvement after correcting with an estimated phase screen are analyzed. Table III summarizes the mean and standard deviation (inside the parenthesis) of the quality parameters azimuth resolution (δ_a), peak-to-sidelobe ratio (PSLR) and integrated sidelobe ratio (ISLR) for the 100 runs. The first row of Table III states the nominal values for an ideal scenario without ionospheric

scintillations, while the second row shows the values when the scintillations are not corrected. The remaining three rows show the results after correcting with FR only, with autofocus only, and with the proposed combined approach, respectively. These results clearly demonstrate that the quality parameters of the azimuth impulse response function can best be improved if the scintillations are estimated with the combined estimation approach.

TABLE II
MEAN (AND STANDARD DEVIATION) OF VARIANCE BETWEEN ESTIMATED AND SIMULATED IONOSPHERIC SCINTILLATIONS FOR 100 RUNS.

	$\text{Var}\{\hat{\varphi} - \varphi\}$
FR estimation	0.301 (0.052)
Autofocus estimation	0.623 (0.659)
Combined estimation	0.183 (0.035)

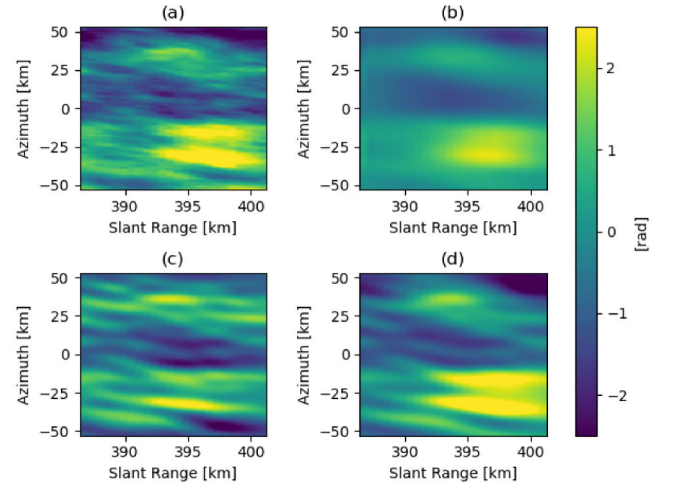


Fig. 1. Performance estimation example with point targets for the different approaches. (a): Simulated phase screen, (b): FR estimation, (c): autofocus estimation, (d): combined estimation.

TABLE III
MEAN (AND STANDARD DEVIATION) OF AZIMUTH RESOLUTION (δ_a), PEAK SIDELobe RATIO (PSLR) AND INTEGRATED SIDELobe RATIO (ISLR) AFTER CORRECTING IONOSPHERIC SCINTILLATIONS WITH DIFFERENT METHODS FOR 100 RUNS.

	δ_a [m]	PSLR [dB]	ISLR [dB]
No scintillations	7.151 (0.035)	-13.204 (0.401)	-10.846 (0.274)
No correction	7.494 (1.463)	-10.703 (3.610)	-7.038 (2.037)
FR correction	7.259 (0.569)	-11.116 (3.182)	-7.461 (1.690)
Autofocus correction	7.272 (0.814)	-10.880 (3.098)	-7.233 (1.854)
Combined correction	7.166 (0.115)	-11.790 (2.596)	-8.194 (1.316)

C. Simulation Results based on Real Airborne Data

The airborne data used in this paper to test the different phase screen estimation methods were acquired during the AFRISAR experiment in Gabon in 2016 [15] with DLR's F-SAR system [16]. This experiment was performed to collect quad-pol radar data of tropical forest at P band to support

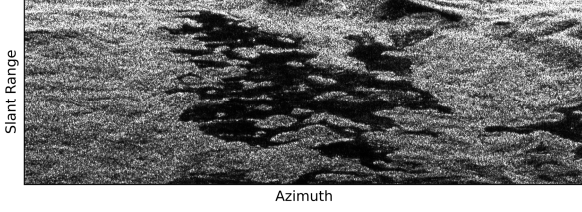


Fig. 2. Multi-look detected image of airborne data adjusted to the quality of the Biomass system (scene size: 3704.5 m \times 5088.0 m).

the Biomass mission. The airborne data were adjusted to the Biomass image quality by reducing the resolution and sampling rate in range and azimuth to the values described in Sections III-A and III-B, degrading the Noise Equivalent Sigma Zero (NESZ) to -28 dB and by injecting ionospheric disturbances (FR and phase screens) to the polarimetric data. The methodology of adjusting airborne data to spaceborne data quality is described in [18]. Figure 2 shows the multi-look detected image of the airborne data adjusted to the quality of the Biomass system. Like in Section III-B, a set of 100 phase screens were simulated and inserted into the data after defocussing the data to the ionospheric height. Note that the azimuth and range extent of an airborne acquisition is much smaller than of a spaceborne one. For this reason, the single-look complex image was stitched together several times in range and azimuth before defocussing to match the size of the simulated phase screen.

Each phase screen was estimated from FR with the Bickel and Bates estimator, which uses the phase difference between the cross-polarized channels of the observed scattering matrix expressed in a circular basis to estimate the FR angle. The relevant equations to estimate the ionospheric phase screen with the Bickel and Bates estimator are found in [5].

In order to improve the shift estimation performance, a multi-look filter was applied to reduce speckle. Here a polarimetric whitening filter as in [19] is used. After multilooking, the phase screens are estimated from autofocus following the same procedure as described in Section III-B. The combined estimation approach is deployed exactly as in Section III-B, but by exploiting the FR and Doppler rate estimation from airborne data. In Figure 3 a flow chart visualizes the combined estimation approach with SAR data.

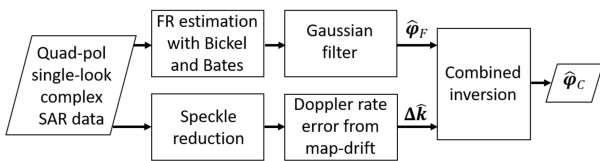


Fig. 3. Flow chart of combined estimation approach with SAR data.

Table IV summarizes the variances between estimated and simulated phase screens of the 100 runs for the three different estimation methods. Table IV shows that, as expected, the lowest variance is achieved with the combined estimation approach.

TABLE IV
MEAN (AND STANDARD DEVIATION) OF VARIANCE BETWEEN ESTIMATED AND SIMULATED IONOSPHERIC SCINTILLATIONS FOR 100 RUNS.

	$\text{Var}\{\hat{\varphi} - \varphi\}$
FR estimation	0.277 (0.037)
Autofocus estimation	0.718 (0.274)
Combined estimation	0.202 (0.023)

TABLE V
MEAN AND STANDARD DEVIATION OF COHERENCE (γ) AND STANDARD DEVIATION OF INTERFEROMETRIC PHASE ($\Delta\phi$) BETWEEN UNDISTORTED DATA AND DATA WITH CORRECTED SCINTILLATIONS ESTIMATED WITH DIFFERENT METHODS FOR 100 RUNS.

	$E\{\gamma\}$	$\sigma\{\gamma\}$	$\sigma\{\Delta\phi\} [\text{rad}]$
No correction	0.725	0.163	1.242
FR correction	0.884	0.066	0.774
Autofocus correction	0.857	0.077	0.979
Combined correction	0.907	0.053	0.703

To evaluate the impact of ionospheric scintillations on the image quality, the coherence and interferometric phase between the undistorted data and the data after applying the different approaches are computed. Table V summarizes the mean ($E\{\cdot\}$) and standard deviation ($\sigma\{\cdot\}$) of the coherence (γ) and the standard deviation of the interferometric phase ($\Delta\phi$) for the 100 runs. The first row of Table V shows the quality parameters for the case where no corrections are applied, while the remaining rows present the results for each estimation approach. In the case of a perfect correction, the mean coherence is equal to one and the standard deviation of the coherence and the interferometric phase are equal to zero. These results show again that the combined estimation approach has the best performance.

For the sake of the example, one out of the 100 realizations is shown in Figures 4 to 6. Figure 4 (a) shows the simulated phase screen while in Figures 4 (b)-(d) display the estimated phase screens. Figures 5 and 6 show the coherence and

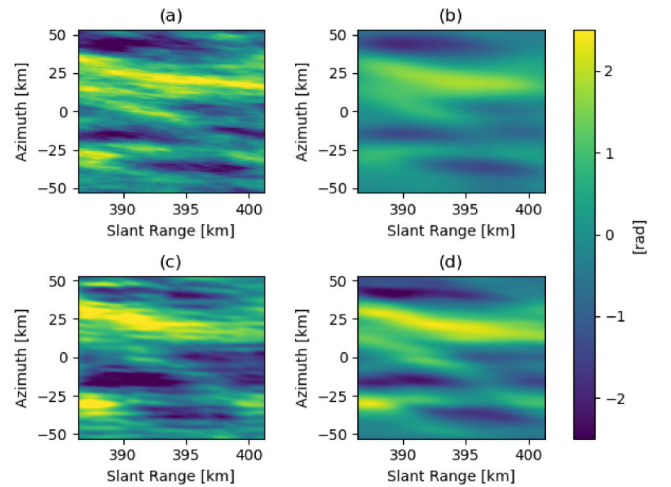


Fig. 4. Performance estimation example with airborne data. (a): Simulated phase screen, (b): FR estimation, (c): autofocus estimation, (d): combined estimation.

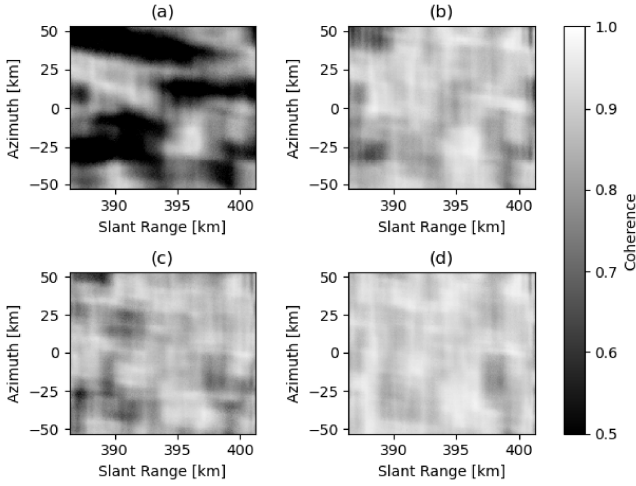


Fig. 5. Coherence between undistorted data and data distorted by the phase screen from Figure 4 (a). (a): No correction applied, (b)-(d): corrected with phase screen from Figure 4 (b)-(d).

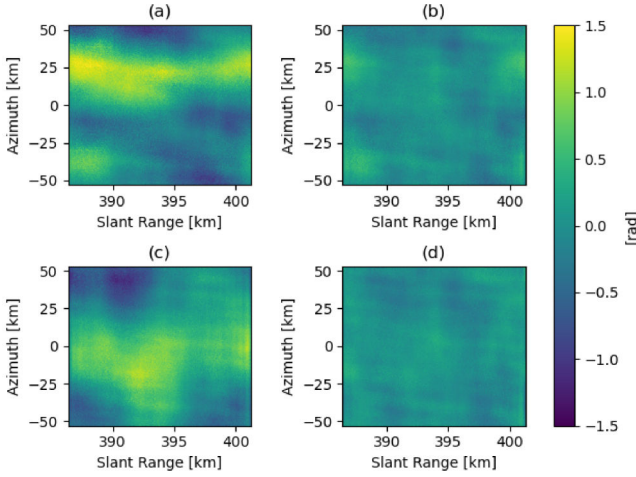


Fig. 6. Interferometric phase between undistorted data and data distorted by the phase screen from Figure 4 (a). (a): uncorrected ionospheric scintillations, (b)-(d): corrected with phase screen from Figure 4 (b)-(d).

interferometric phases for this particular realization. Figures 5 (a) and 6 (a) display the results without applying any correction, and Figures 5 (b)-(d) and 6 (b)-(d) show the improvements after applying the correction corresponding to each estimation approach. These results show qualitatively that the combined approach minimizes the residual error.

IV. CONCLUSION

Uncorrected ionospheric scintillations can have a non-negligible impact on the quality of SAR images. In this paper, a novel estimation technique that exploits FR and map-drift autofocus has been proposed and validated. Simulation results with point targets and adapted airborne P-band data demonstrate the superior performance of the proposed combined

approach when compared to using FR and map-drift autofocus independently. The performance of the combined estimation approach will however also depend on the performances of the single estimation approaches. The performance of the FR estimation approach varies with the latitude and the correlation length of the scintillations, while the map-drift autofocus performs only well if the scene has enough texture.

REFERENCES

- [1] D. P. Belcher, "Theoretical limits on SAR imposed by the ionosphere", *IET Radar, Sonar and Navigation*, vol. 2, no. 6, pp. 435-448, 2008.
- [2] J. Aaron, "Global morphology of ionospheric scintillation", *Proc. IEEE*, vol. 70, no. 4, pp. 360-378, 1982.
- [3] N. C. Rogers, S. Quegan, J. S. Kim and K. P. Papathanassiou, "Impacts of ionospheric scintillation on the BIOMASS P-band satellite SAR", *IEEE Transactions on Geoscience and Remote Sensing*, vol. 52, issue 3, pp. 1856-1868, 2014.
- [4] Z. Li, S. Quegan, J. Chen and N. C. Rogers, "Performance analysis of phase gradient autofocus for compensating ionospheric phase scintillation in BIOMASS P-band SAR data", *IEEE Geoscience and Remote Sensing Letters*, vol. 12, no. 6, pp. 1367-1371, 2015.
- [5] J. S. Kim, K. P. Papathanassiou, R. Scheiber and S. Quegan, "Correcting distortion of polarimetric SAR data induced by ionospheric scintillation", *IEEE Transactions on Geoscience and Remote Sensing*, vol. 53, issue 12, pp. 6319-6335, 2015.
- [6] P. Prats-Iraola et al., "The BIOMASS ground processor prototype: An overview", *12th European Conference on Synthetic Aperture Radar (EUSAR)*, Aachen, Germany, 2018.
- [7] G. Gomba and F. De Zan, "Bayesian data combination for the estimation of ionospheric effects in SAR interferograms", *IEEE Transactions on Geoscience and Remote Sensing*, vol. 55, issue 11, pp. 6582-6593, 2017.
- [8] S. H. Bickel and R. T. H. Bates, "Effects of magneto-ionic propagation on the polarization scattering matrix", *Proc. IEEE*, vol. 53, no. 8, pp. 1089-1901, 1965.
- [9] C. L. Rino, "On the application of phase screen models to the interpretation of ionospheric scintillation data", *Radio Sci.*, vol. 17, no. 4, pp. 855-867, 1982.
- [10] I. Cumming and F. Wong, "Digital processing of synthetic aperture radar data", *Artech House*, Norwood, MA, 2005.
- [11] C. L. Rino, "The theory of scintillation with applications in remote sensing", *Hoboken, NJ, USA: Wiley*, 2011.
- [12] D. L. Knepp, "Multiple phase-screen calculation of the temporal behaviour of stochastic waves", *Proc. of IEEE*, vol. 71, no. 6, pp. 722-737, 1983.
- [13] C. L. Rino, "A Power law phase screen model for ionospheric scintillation: 1. weak scatter", *Radio Sci.*, vol. 14, no. 6, pp. 1135-1145, 1979.
- [14] E. J. Fremouw and J. A. Secan, "Modeling and scientific application of scintillation results", *Radio Science*, vol. 19, no. 3, pp. 687-694, 1984.
- [15] I. Hajnsek, M. Pardini, R. Horn, R. Scheiber, M. Jaeger, M. Keller, D. Gesswein, K. Papathanassiou and A. Reigber, "3-D SAR imaging of African forests: Results from the AfriSAR Campaign at P- and L-band", *11th European Conference on Synthetic Aperture Radar (EUSAR)*, Hamburg, Germany, 2016.
- [16] A. Reigber, R. Scheiber, M. Jaeger, P. Prats, I. Hajnsek, T. Jagdhuber, K. P. Papathanassiou, M. Nannini, E. Aguilera, S. Baumgartner, R. Horn, A. Nottensteiner and A. Moreira, "Very-high-resolution airborne synthetic aperture radar imaging: Signal processing and applications", *Proceedings of the IEEE*, vol. 101, no. 3, 2013.
- [17] J. A. Secan, R. M. Bussey, E. J. Fremouw, and S. Basu, "High-latitude upgrade to the wideband ionospheric scintillation model", *Radio Science*, vol. 32, no. 4, pp. 1567-1574, 1997.
- [18] R. Scheiber, S.-K. Lee, K. P. Papathanassiou and N. Floury, "Extrapolation of airborne polarimetric and interferometric SAR data for validation of bio-geo-retrieval algorithms for future spaceborne SAR missions", *Proc. IGARSS*, Cape Town, South Africa, 2009.
- [19] J.-S. Lee, M. R. Grunes and S. A. Mango, "Speckle reduction in multi-polarization, multifrequency SAR imagery", *IEEE Trans. on Geoscience and Remote Sensing*, vol. 29, no. 4, pp. 535-544, 1991.